metals

MDPI

Article

The Corrosion Behaviour of Additively Manufactured AlSi10Mg Parts Compared to Traditional Al Alloys

Andrea Gatto [1], Camilla Cappelletti [1], Silvio Defanti [1,*] and Fabrizio Fabbri [2]

[1] Department of Engineering "Enzo Ferrari", University of Modena and Reggio Emilia, Via Vivarelli 10, 41125 Modena, Italy; andrea.gatto@unimore.it (A.G.)
[2] Ferrari S.p.A., Via Abetone Inferiore 4, 41053 Maranello, Italy
* Correspondence: silvio.defanti@unimore.it

Abstract: Additive manufacturing of metal parts in the motorsport industry is becoming a decisive technology for producing lightweight and rigid parts, with increasing applications as the costs decrease. Among the available metal alloys, AlSi10Mg is one of the most widely used. In this paper, the corrosion resistance of additively manufactured AlSi10Mg is compared with that of other traditionally manufactured aluminium alloys widespread in the automotive industry. Several potentially corrosive agents, typical of vehicle applications, were used: salty water, motor oil, suspension oil, cooling fluid and gasoline. Corrosion tests were conducted at both room temperature and 90 °C. The effects of heat and surface treatments were evaluated separately. The samples were visually inspected and weighed to evaluate the corrosion rate with the aid of SEM and EDS analysis. Additively manufactured AlSi10Mg generally showed better corrosion resistance in the stress-relieved condition as compared to the T6-treated state, with slightly better results for the polished samples. Motor oil, suspension oil, cooling fluid and gasoline did not significantly corrode the specimens, except for the T6-treated AlSi10Mg samples at 90 °C. However, the corrosion rate was always higher than traditionally manufactured aluminium alloys tested for comparison.

Keywords: laser powder bed fusion; AlSi10Mg; corrosion resistance; corrosion rate

Citation: Gatto, A.; Cappelletti, C.; Defanti, S.; Fabbri, F. The Corrosion Behaviour of Additively Manufactured AlSi10Mg Parts Compared to Traditional Al Alloys. *Metals* **2023**, *13*, 913. https://doi.org/10.3390/met13050913

Academic Editor: Eric Hug

Received: 11 April 2023
Revised: 4 May 2023
Accepted: 5 May 2023
Published: 8 May 2023

1. Introduction

Additive manufacturing (AM) technology, especially Laser-Based Powder Bed Fusion (L-PBF), is becoming increasingly important in various industries [1]. L-PBF is a process that uses a laser source to selectively melt metal powder, building up the component layer by layer [2]. The main advantages of this technology are the reduction in scrap material and the possibility to produce components with geometries that are otherwise not feasible [3,4]. This enables the redesign of components with a view to improving functionality and optimizing weight [5].

These are the main reasons why various industrial sectors, such as automotive, have an increasing interest in AM. Among all aluminium alloys, AlSi10Mg is one of the most widely used, thanks to its properties in terms of processability, low weight, low cost and high mechanical properties [6,7]. This is related to the high cooling rates typical of the L-PBF process, leading to an extremely fine microstructure characterized by supersaturated silicon in a solid solution in the Al matrix [8,9]. On the other hand, the exceptionally rapid cooling leads to significant residual stresses in the printed part [10]. Therefore, the parts are generally heat treated to reduce the internal stresses while maintaining good mechanical properties [10]. In addition, to eliminate anisotropy due to the layer-by-layer nature of the AM process, T6 heat treatment is often applied [11]. The microstructure is greatly altered by the solution heat treatment at high temperatures. The excess Si precipitates out and starts to coarsen while it is uniformly distributed in the Al matrix [6,12].

For automotive applications, the working environment of the printed components must also be considered in the design phase. In particular, the corrosion resistance of the

alloy in different environments must be carefully evaluated. Several studies have been conducted on this topic [13–15], with particular attention paid to the corrosion resistance of Al-Si AM parts in salty water [16]. Yang et al. found that in the absence of heat treatment, microgalvanic pairs form between the small cathode, represented by the Si network in the as-printed microstructure and the large anode (the Al matrix). This phenomenon leads to the formation of a protective oxide film on the component surface, which hinders the corrosion propagation and accounts for the high corrosion resistance of Al-Si AM parts [17]. After the application of T6 heat treatment, the microstructure changes into Si particles that are uniformly distributed in the aluminium matrix, which promotes corrosion advance and reduces the corrosion resistance of the part [18]. All the studies considered deal only with corrosion in salt water at room temperature, while the effects of higher operating temperatures or contact with various liquids have not yet been reported.

Another important factor affecting the corrosion behaviour of a part is its surface finish. In general, the higher the surface roughness, the lower the corrosion resistance [19]. On this topic, Leon et al. have demonstrated the better corrosion behaviour of polished AM AlSi10Mg specimens, compared to as-printed ones [20].

The aim of this study is to deepen the corrosion analysis of AM AlSi10Mg components by considering different conditions and environments. AlSi10Mg specimens were subjected to various heat and surface treatments to evaluate their combined effects on corrosion resistance. The results were compared with those of conventional aluminium alloys produced by casting and bulk deformation. All alloys were tested by immersion in various fluids commonly used in the automotive sector to evaluate their behaviour in the actual working environment.

2. Materials and Methods

The additive specimens were printed using an SLM 500 machine (SLM Solution GmbH, Germany). The machine was equipped with four overlapping IPG fiber lasers operating simultaneously, with each laser capable of a maximum power of 400 W and an estimated beam focus diameter between 80 and 115 microns. During the process, argon with a purity of approximately 99.998% flowed into the build chamber to ensure an inert environment with an oxygen content of less than 0.1%, thus, reducing the risk of oxide formation within the printed parts. The SLM supplied AlSi10Mg powder with the chemical composition listed in Table 1.

Table 1. AlSi10Mg powder and A356 aluminium alloy nominal compositions (weight %).

Alloy	Al	Si	Cu	Mn	Mg	Zn	Fe
AlSi10Mg powder	Balance	9–11	≤0.05	≤0.45	0.2–0.45	≤0.1	≤0.55
A356—Sand casting	Balance	6.5–7.7	≤0.03	≤0.10	0.35–0.45	≤0.03	≤0.15

Blocks of 100 × 50 × 5 mm were printed with a layer thickness of 60 µm, with the longer side oriented perpendicularly to the build platform. The specimens were subjected to different heat treatments, namely stress-relieving (SR) and T6, to investigate the corrosion resistance for different microstructures. The SR treatment consisted of 300 °C for 2 h, while T6 consisted of a solubilization above 510 °C, quenching in hot water and aging at 150 °C for 4.5 h.

To evaluate the possible influence of surface roughness on the corrosion resistance of the AlSi10Mg L-PBF parts, all specimens were tested both in the as-built non-machined (NM) condition and in the surface-polished condition (PO). In this regard, the Tegramin-30 automatic polishing machine (Struers Inc., Cleveland, OH, USA) was used with up to a fine 1200 SiC abrasive paper. Moreover, two other finishing processes were applied to some of the AlSi10Mg samples subjected to stress relief: sand blasting (SB) with corundum and DryLyte® (GPAINNOVA, Barcelona, Spain) (DLT) treatment. The latter is an electrochemical process in which small spheres act as the electrolyte for an electrolysis reaction [21]. The part acts as the anode, i.e., when the process is activated, the electric current starts to flow

and produces an oxidized layer, which is subsequently dissolved, leaving a smooth surface. The surface roughness was measured on the samples prior to corrosion testing. Areas of 2.3 × 2.7 mm^2 were scanned with an S Neox confocal microscope (Sensofar, Barcelona, Spain), a planar filter was applied for form removal, and the average surface roughness was measured.

For direct comparison, A356 specimens with the chemical composition listed in Table 1 were obtained by sand casting and T6 treated. Again, some of the specimens were left unmachined (NM), while others were polished (PO) with SiC abrasive paper to 1200 grit. Other alloys from bulk deformation were also tested:

- 6082 T6 (extrusion)
- 5083 O (superplastic forming)
- 1050 H24 (superplastic forming)
- 3003 H111 (lamination)

These specimens were only considered in the NM condition, since automotive applications generally do not involve finishing after the bulk deformation processes are considered. Table 2 gives the complete set of alloys tested and their manufacturing methods, heat treatments and surface finishing.

Table 2. Tested samples, alloys and their manufacturing technique, and heat and surface treatments. Abbreviation legend: AM—additive manufacturing, SR—stress relief, NM—non-machined, PO –polished, SB—sand blasted, and DLT—DryLyte® treated. For traditionally produced alloys, the designation is given according to the standard ANSI H35.1 [22].

Sample ID	Material	Manufacturing Technique	Thermal Treatment	Surface Finishing
AlSi10Mg_SR_NM	AlSi10Mg	AM	SR	NM
AlSi10Mg_SR_PO	AlSi10Mg	AM	SR	PO
AlSi10Mg_SR_SB	AlSi10Mg	AM	SR	SB
AlSi10Mg_SR_DLT	AlSi10Mg	AM	SR	DLT
AlSi10Mg_T6_NM	AlSi10Mg	AM	T6	NM
AlSi10Mg_T6_PO	AlSi10Mg	AM	T6	PO
A356_T6_NM	A356	Sand Casting	T6	NM
A356_T6_PO	A356	Sand Casting	T6	PO
6082_T6_NM	6082	Extrusion	T6	NM
5083_O_NM	5083	Superplastic Forming	O	NM
1050_H24_NM	1050	Superplastic Forming	H24	NM
3003_H111_NM	3003	Laminated	H111	NM

Prior to the corrosion testing, microstructural analyses were performed on the AlSi10Mg (SR and T6) as well as on the cast A356 T6 specimens. The sections were polished using up to a fine 0.25 µm silica suspension and then etched with Keller reagent. The AlSi10Mg samples were sectioned along the XY and Z planes, respectively, parallel and perpendicular to the layers in the L-PBF process.

Two types of corrosion tests were carried out:

- Partial immersion in saline water (NaCl 5 wt%) for 30 days for a preliminary visual check of the possible corrosion phenomena.
- Full immersion of the samples in several fluids to calculate the corrosion rate.

For the latter tests, the samples were immersed for 30 days at room temperature in the following fluids:

- Saline water (NaCl 5%);
- 5W40 oil;
- Oil for active suspensions;
- Cooling fluid (50% distilled water and 50% glycol);

- Automotive gasoline.

The immersion tests in 5W40, oil for active suspensions and water-glycol (50%) were also performed at T = 90 °C to simulate the in-vehicle environment. Table 3 sums up the immersion test conditions.

Table 3. Fluids selected for corrosion tests and corresponding temperatures.

Fluids	Test Temperature [°C]
Saline water	20
5W40 oil	20, 90
Suspension oil	20, 90
Cooling fluid	20, 90
Gasoline	20

All specimens were photographed before and after the corrosion testing to visually evaluate signs of corrosion on the surfaces. After visual inspection, the samples were sectioned near the corrosion sites. The sections were then polished using up to a fine 0.25 µm silica suspension and then etched with Keller reagent. The morphologies of the corroded surfaces and compositions of the corrosion products were further analyzed with a scanning electron microscope (ZEISS Sigma 300 VP).

In order to achieve quantitative, objective results, the corrosion rate was calculated after the immersion tests, according to the standard ASTM G31-72 [23–25]. Equation (1) gives the micrometers of corroded material per year:

$$Corrosion\ rate = \frac{K \cdot W}{A \cdot T \cdot D} \left[\frac{\mu m}{year}\right] \quad (1)$$

where:

- $K = 8.76 \cdot 10^7$ is an adimensional constant;
- W is the weight loss [g];
- A is the sample area in contact with the fluid [cm^2];
- T is the test duration [hours];
- D is the material density [g/cm^3].

A notable limitation of the above definition is that it considers corrosion to be homogenous all over the surfaces in contact with the fluid in which the sample is immersed; however, the application of the procedure according to this standard ensures the repeatability of the results.

To correctly calculate the corrosion rate, each specimen was properly prepared by cutting it to dimensions of 25 mm × 50 mm × 5 mm and then cleaning it with an organic solution and weighing it before and after the corrosion tests using a Sartorius analytical scale with a resolution of 0.1 mg. Special attention was paid to the cleaning of the AlSi10Mg as-built specimens. These samples were repeatedly ultrasonically cleaned to ensure the complete removal of any unmelted powders adhering to the raw surface. This procedure avoided the risk of overestimating the mass loss.

After the testing, the samples surfaces were cleaned of the corrosion products according to ASTM G1-03 [26] by repeating multiple steps of immersion in nitric acid (HNO^3) at a concentration of 69%, followed by immersion in an organic solution and ultrasonic cleaning. The standard suggests repeating multiple cleaning cycles to have better control over the weight loss. The mass loss should be plotted against the number of cleaning steps performed, until a curve is obtained as in Figure 1. The flat segment corresponds to the beginning of the removal of the bulk material during the cleaning process, which means that all the corrosion products have been eliminated. The mass loss value to be used in Equation (1) is represented by point B.

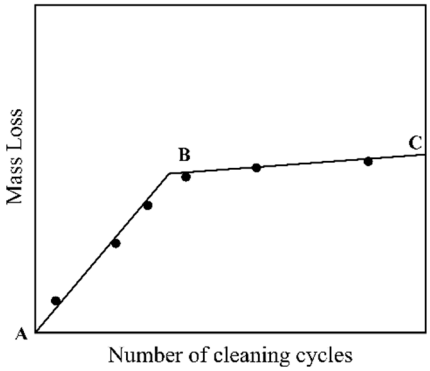

Figure 1. Mass loss after immersion corrosion tests as a function of the number of cleaning cycles, according to ASTM G1-03.

3. Results and Discussion

3.1. Microstructure

Figure 2 shows the microstructure along the Z direction of the AlSi10Mg_SR_NM samples. Melt pools representative of the layer-by-layer laser scanning strategy can be seen, including their contour and core areas. The distinguished layers confirm the material's anisotropy, as it is known that the application of a stress-relief anneal leaves the melt traces unchanged [27]. The small dark spots are residual pores.

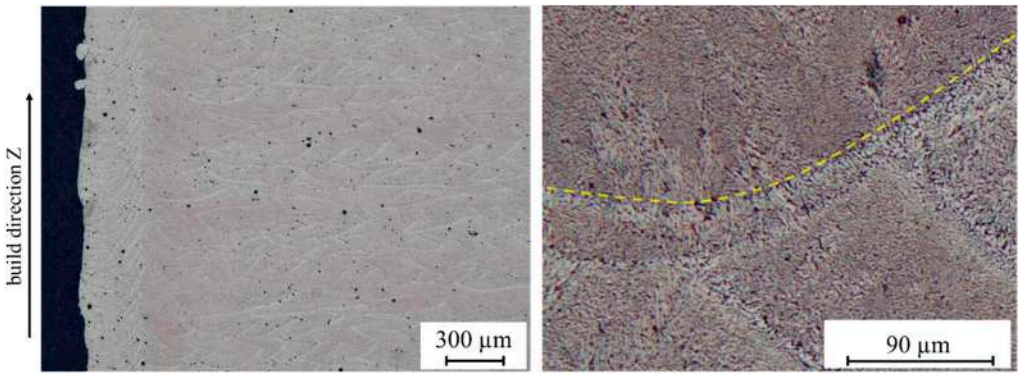

Figure 2. Microstructure of AlSi10Mg_SR_NM specimens in a section parallel to the printing direction. The yellow dashed line highlights one of the melt pool boundaries.

At the boundaries of the melt pools, the microstructure became coarser with the enlargement of the α-Al islands and an initial rupture of the Si network, similar to what has been observed by other authors [28,29].

The SEM observation of the AlSi10Mg_SR_NM processed by L-PBF (Figure 3) is consistent with the literature. The extremely fast cooling rates in the range of 10^3–10^8 K/s [30] caused a cellular-dendritic solidification mechanism. Two distinct phases were obtained: a cellular-dendritic α-Al phase, rich in aluminium with dispersed Si (the grey islands in Figure 3), and a eutectic Al-Si phase, rich in Si and poor in Al [20], represented by the lighter grid. Observation of the sections along the Z-build direction (Figure 3a) and parallel to the layers (Figure 3b) reveals that the grains are elongated along the Z axis.

The application of T6 heat treatment resulted in a profound change in the microstructure (Figure 4). The solution treatment broke the Si interconnected structure, which is typical of a microstructure in the as-built or stress-relieved state. The Si domains begin to coarsen and, therefore, decrease in density [6,31,32]. The Si areas become uniformly distributed in the Al matrix, where melt pools and melt traces are no longer visible and the microstructure becomes homogeneous.

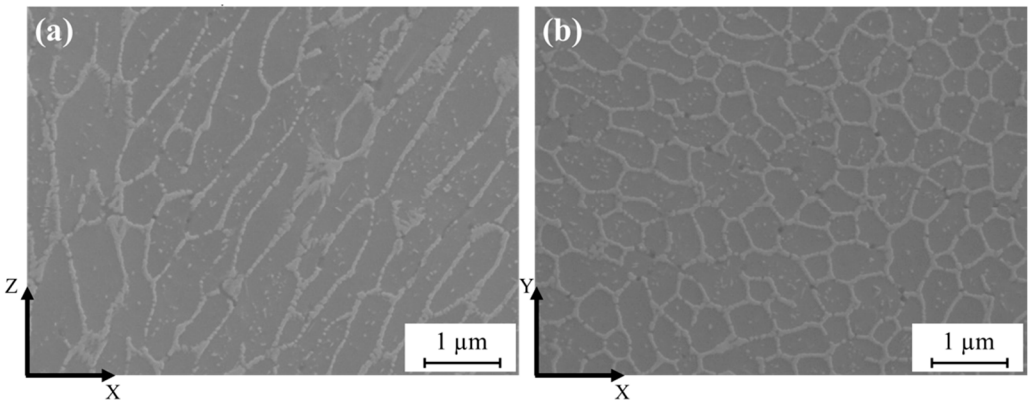

Figure 3. AlSi10Mg_SR_NM microstructure, characterized by the α-Al matrix and surrounded by eutectic the Al-Si phase (lighter grid). (**a**) Section parallel to build direction Z and (**b**) perpendicular to build direction.

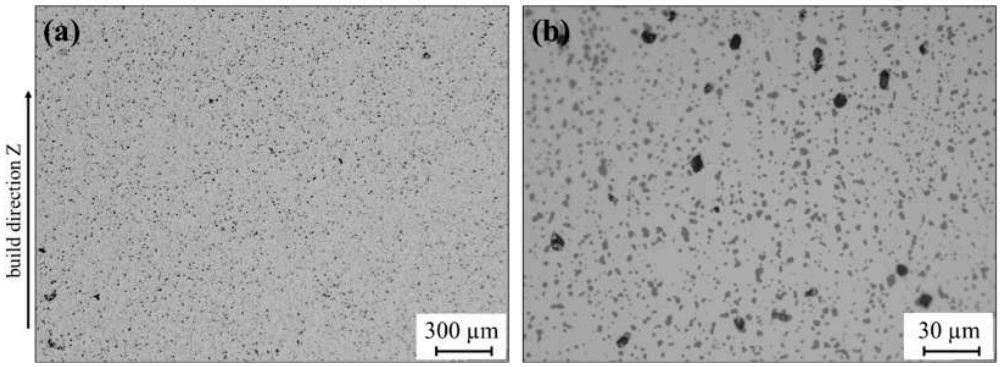

Figure 4. Microstructure of AlSi10Mg_T6_NM additive manufactured sample. (**a**) lower, and (**b**) higher magnification. The melt pools are not distinguishable, and the Si domains are uniformly distributed in the Al matrix. The small black spots are residual pores.

The microstructure of the sand-cast A356_T6_NM aluminium was characterized by the typical dendritic Al phase [33,34], shown by the light areas in Figure 5.

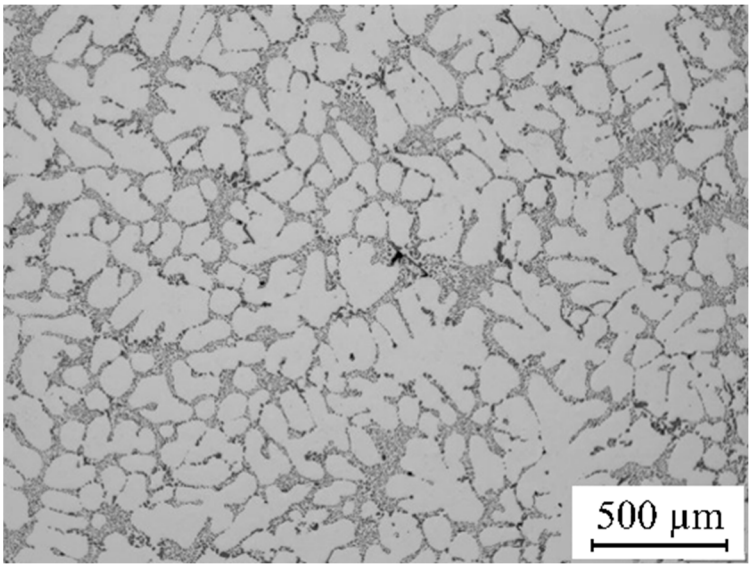

Figure 5. Microstructure of cast A356_T6_NM specimen.

3.2. Immersion Tests in NaCl 5%

The average surface roughness of the S_a resulted to be 10 µm in the NM condition, 9 µm after sand blasting, 6 µm for the DLT specimens and 0.3 µm for the polished ones. First, the samples were partially immersed in saline water for a visual inspection of the corrosion phenomena.

3.2.1. AM: NM Samples

Figure 6a shows the AlSi10Mg_SR_NM samples before and after the partial immersion test. The red rectangles highlight the immersed portion. In the AlSi10Mg_T6_NM samples (Figure 6b), the corrosion phenomenon is more marked, especially at the liquid-air interface, where the presence of oxygen made the environment harsher.

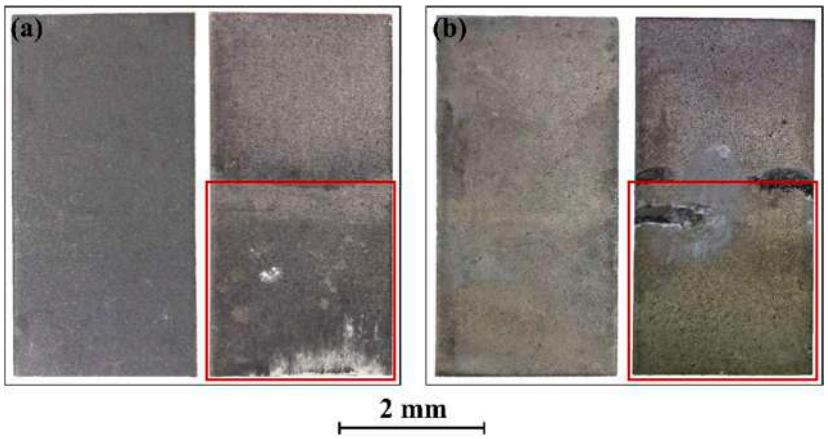

Figure 6. Visual comparison of (**a**) AlSi10Mg_SR_NM and (**b**) AlSi10Mg_T6_NM specimens before and after partial immersion in NaCl (5%).

Stress-relieved samples were characterized by the deposition of corrosion products on the specimen surface. SEM observation confirmed the presence of aluminium oxides, as demonstrated by EDS analysis (Figure 7).

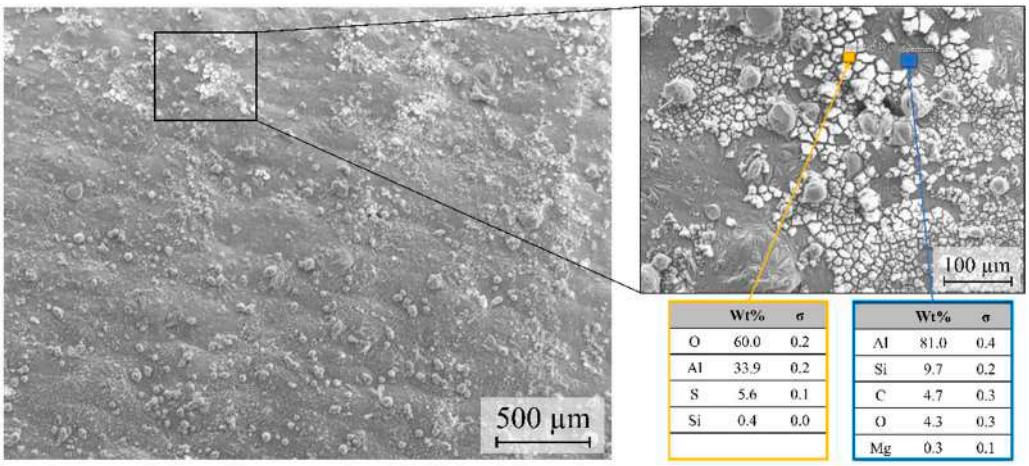

Figure 7. SEM and EDS analyses of corrosion products found on the AlSi10Mg_SR_NM specimen after immersion for 30 days in NaCl (5%).

The same area was further examined by sectioning and etching the sample to reveal the microstructure. As can be seen in Figure 8, the corrosion progressed in the sample by selectively removing material from the edges of the molten pool borders, which were more reactive than the centre. This behaviour is due to the coarser microstructure and partial rupture of the Si network at the melt pool boundaries, leading to rapid corrosion of the

α-Al [17,18]. Therefore, the disruption of the Si network facilitates corrosion along the melt pool boundaries. At the same time, the progression of corrosion towards the centre of the melt pool can be hindered by the fine microstructure and the supersaturated α-Al phase, where the increased presence of Si in solid solution (due to the high solidification rate in the L-PBF process) guarantees higher corrosion resistance.

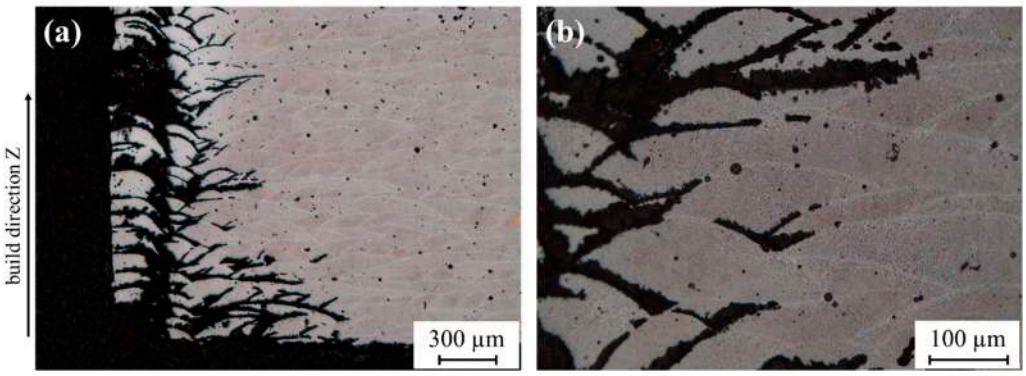

Figure 8. Corrosion propagation along melt pool boundaries on AlSi10Mg_SR_NM specimens. (**a**) lower, and (**b**) higher magnification.

The SEM and EDS analyses (Figure 9) confirmed that alumina is deposited on the deeply corroded surfaces of the AlSi10Mg_T6_NM samples.

The sample was sectioned at the liquid-air interface to assess the extent of the corrosion. Figure 10 shows that the corrosion was not confined to the melt pool borders but rather proceeded more diffusely through the sample. This mechanism is different from that observed in the SR specimens because of the different microstructure obtained after the solution annealing. The loss of corrosion resistance observed in the SR samples at the melt pool boundaries was more severe in this case and spread to the entire specimen. As the Si domains became uniformly distributed in the Al matrix and the continuous network was broken, while the overall microstructure became coarser, a broader and more homogeneous corrosion reaction occurred to the aluminium matrix.

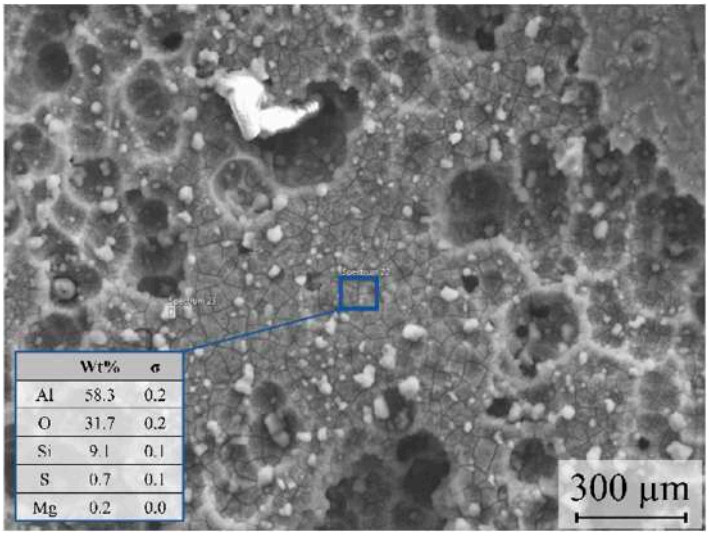

Figure 9. SEM and EDS analyses of the AlSi10Mg_T6_NM specimen after immersion test in NaCl (5 wt%) in the zone of the liquid-air interface. The surface is covered by aluminium oxide and is widely corroded.

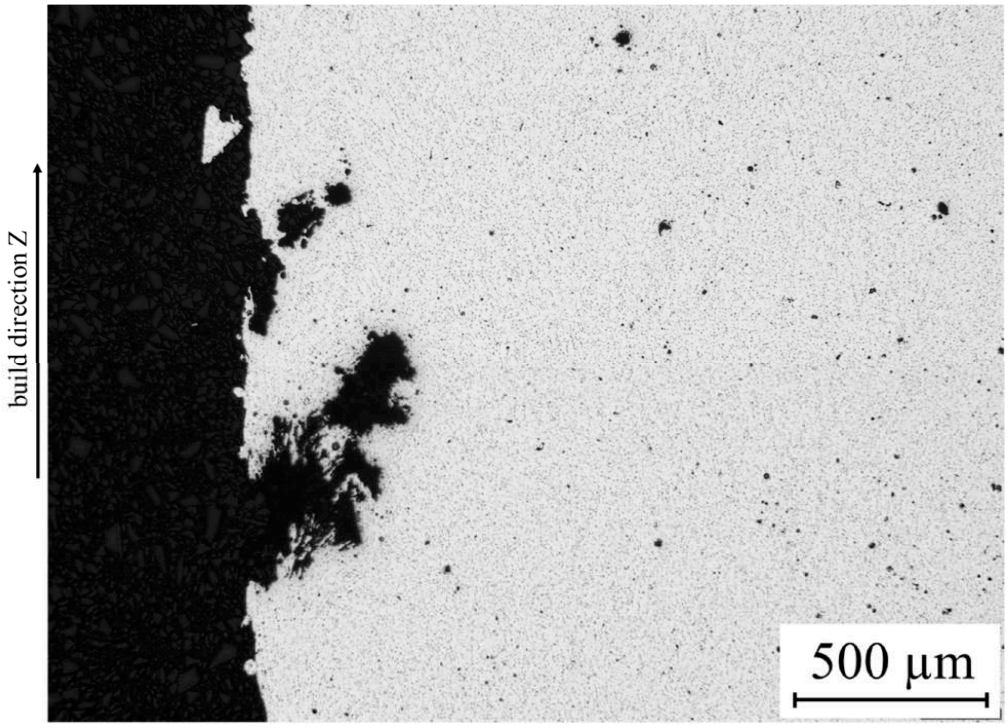

Figure 10. Section of the AlSi10Mg_T6_NM specimen after immersion test in NaCl (5%). The corrosion advanced inside the sample for 0.5 mm.

3.2.2. AM: Finished Samples

Figure 11 shows the results of the partial immersions of AlSi10Mg_SR_DLT and AlSi10Mg_SR_SB in NaCl (5%). Both exhibited widespread oxidation on the immersed areas, with local deposition of corrosion products.

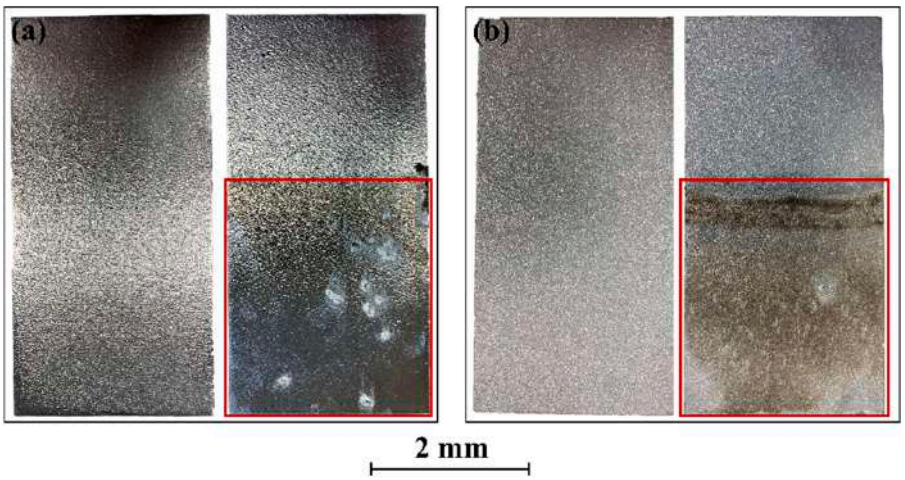

Figure 11. Visual comparison of (**a**) AlSi10Mg_SR_DLT and (**b**) AlSi10Mg_SR_SB before and after partial immersion in NaCl (5%).

As for the DLT specimen, the finishing process itself seemed to promote local corrosion. In fact, the DLT process may have exposed porosities located under the sample skin that may have served as preferential sites for the onset of corrosion. This hypothesis was confirmed by the SEM images in Figure 12, which show the surface morphology before and after the immersion test. It can be seen that DLT prior to immersion resulted in a generally smooth surface with localised circular craters corresponding to pre-existing porosities

exposed by the finishing operation (Figure 12a). Figure 12b shows a preferential deposition of corrosion products in the described pores.

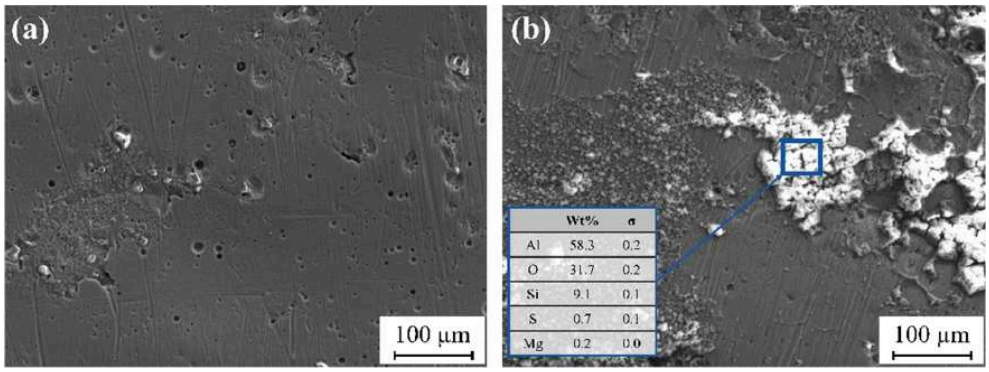

Figure 12. SEM and EDS analyses of the AlSi10Mg_SR_DLT specimen (**a**) before and (**b**) after 30 days of immersion in NaCl (5%).

Analyses of the metallographic sections of the two surface-finished specimens (Figure 13) displayed the mechanism of corrosion propagation already described in Figure 8 for the specimens from SR. Even in this case, the corrosion proceeded along the melt pool boundaries. However, the DLT specimen exhibited deeper corrosion that extended beyond the thickness of the sample that was built during L-PBF using the contour strategy and reached the sample core. On the contrary, for the SB sample, the corrosion stopped within the contour region without progressing further. This could be due to the closure of defects as a result of plastic deformation during the sand blasting, reducing the number of sites where corrosion could begin. The protective effect of sand blasting could also be due to the compressive stress state due to the slight work hardening at the surface of the specimen.

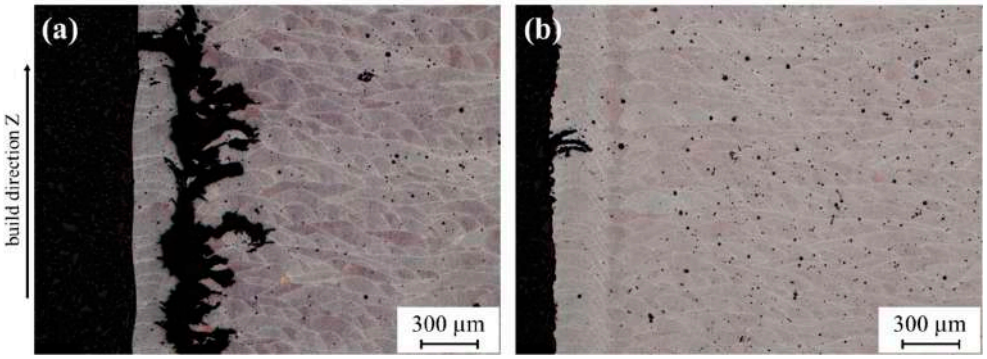

Figure 13. Corrosion propagation on (**a**) AlSi10Mg_SR_DLT and (**b**) AlSi10Mg_SR_SB specimens. In both the specimens, corrosion selectively occurs at the melt pool borders.

Figure 14a shows the corroded surface of the AlSi10Mg_T6_PO. In comparison to the NM conditions, the polishing process provides much higher corrosion resistance. Figure 14b suggests a similar result for the A356_T6_PO. The corrosion behaviour of this alloy in the NM state is discussed further in the following section.

3.2.3. Other Alloys

The corrosion behaviour of the aluminium alloys produced using traditional methods is shown in Figure 15. The A356_T6_NM (Figure 15a,b) showed the worst corrosion resistance, with clear signs of pitting. In the presence of shrinkage porosities emerging at the surface, the corrosion progressed rapidly by selective removal of the interdendrite phase. As a result of the surface defects, the corrosion was much more severe in the NM cast alloy than in the additively manufactured samples in the same condition.

Among the wrought alloys, metallographic analyses of alloys 5083 (Figure 15d), 1050 (Figure 15e) and 3003 (Figure 15f) showed no signs of corrosion, while alloy 6082 (Figure 15c) was characterized by slight corrosion at the air-liquid interface.

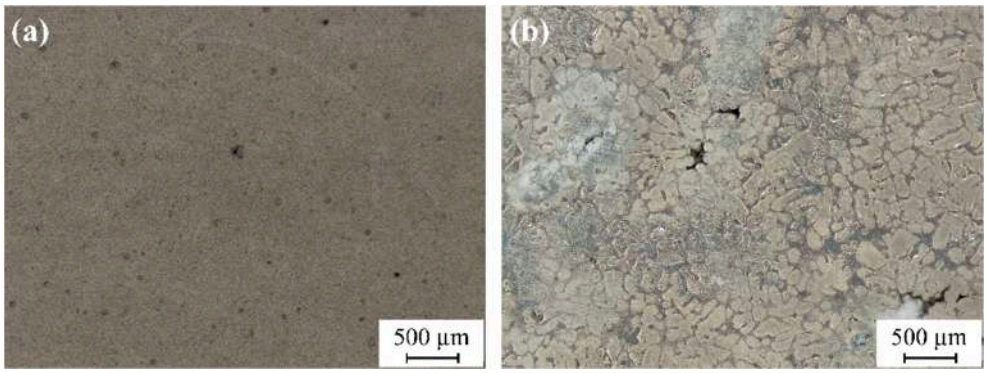

Figure 14. Surfaces of (**a**) AlSi10Mg_T6_PO and (**b**) A356_T6_PO specimens.

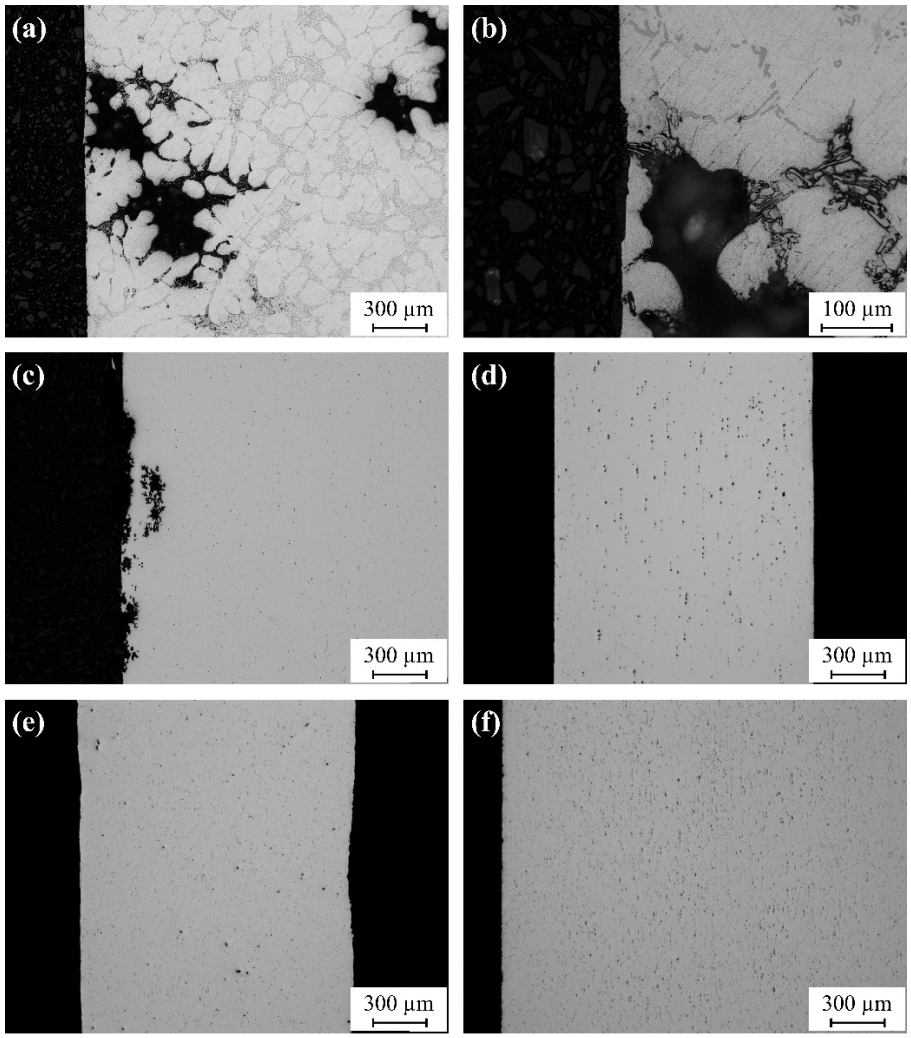

Figure 15. Metallographic sections of (**a**,**b**) A356_T6_NM, (**c**) 6082_T6_NM, (**d**) 5083_O_NM, (**e**) 1050_H24_NM and (**f**) 3003_H111_NM specimens after immersion in NaCl (5%) for 30 days.

3.2.4. Corrosion Rate Quantification

In addition to visual inspection, the corrosion behaviour was determined numerically by calculating the corrosion rate for specimens completely immersed in NaCl (5%) at room

temperature. The graph in Figure 16 shows the results measured according to ASTM G31-72 [23]. The AM AlSi10Mg samples exhibited higher corrosion resistance than the A356_T6_NM specimens obtained by sand casting, regardless of surface finish and heat treatment. The reason for this poorer corrosion behaviour of the A356 alloy can be related to the corrosion phenomena described earlier. The protective effect of the fine and continuous Si network in the AlSi10Mg AM specimens provides higher corrosion resistance compared to the A356-cast samples, where the typical cast dendritic microstructure is generally coarser and has broad Al matrix regions that are more susceptible to corrosion [12].

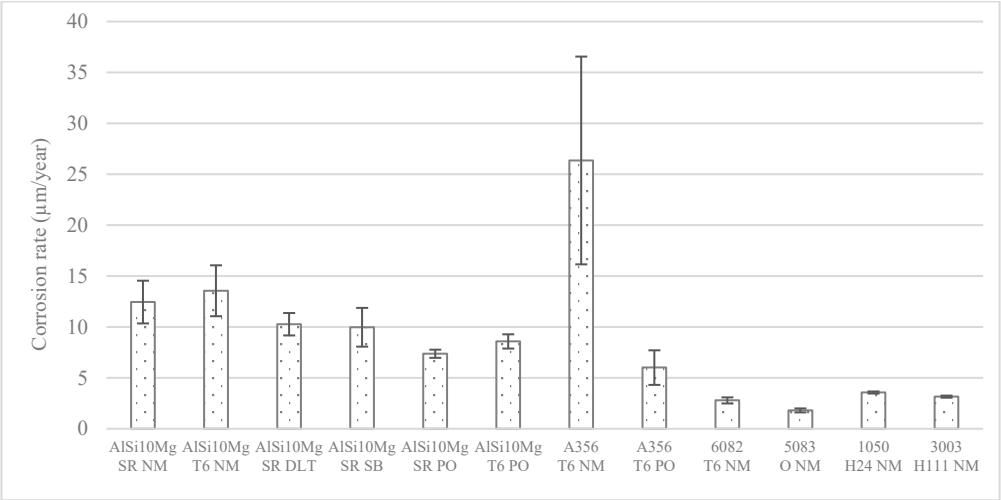

Figure 16. Corrosion rate measurements for all the tested specimens after complete immersion in NaCl (5%) for 30 days.

Focusing on the AlSi10Mg samples, it is observed that the application of surface finishing resulted in an improvement of the corrosion resistance, compared to the non-machined specimens. This result could be explained by the reduction in the corrosion trigger points associated with obtaining a smoother surface. The qualitative effect previously observed for the DLT process, which caused a rapid progression of corrosion beyond the contour thickness, becomes extremely minor in terms of the quantitative results. The difference between the corrosion rates of SB and DLT specimens was only 3%. This result could be explained by conjecturing that corrosion occurs on the SB surfaces in more numerous, albeit shallower, locations than on the surfaces finished by DLT. Corrosion is extremely severe at the pores exposed by DLT (Figure 13a), but these sites are so sporadic that they only affect the quantitative measurement by 3%.

The above considerations are supported by the results achieved for the polished samples, which showed the highest corrosion resistance among the surface conditions examined. This is consistent with the results in the literature. For example, Leon et al. [20] observed significantly lower corrosion resistance for unmachined, compared to polished, additively manufactured parts. This result is attributed to the higher surface roughness and more frequent surface cavities on the unmachined specimens.

As for the effect of the heat treatments, according to the results, T6 led to a slightly higher corrosion rate in comparison to SR. This is in agreement with the wide and pervasive corrosion observed on the metallographic sections, as well as with other studies. For example, in another research study, Leon et al. [35] performed immersion tests in NaCl (3.5%) and measured greater weight losses for T6 specimens than for stress-relieved or as-printed samples.

Overall, both the AM and cast parts were characterized by a higher corrosion rate compared to the wrought aluminium alloys under all conditions investigated.

3.3. Immersion Tests in 5W40, Suspension Oil, Cooling Fluid and Gasoline at Room Temperature

After the 30-day immersion tests in the various liquids, none of the specimens showed any morphological changes on the surface, indicating that corrosion did not occur on any of the tested samples.

The corrosion rate measurements confirmed the result of the visual inspections. The selected Al specimens in 5W40, oil for active suspensions, glycol (50%) and automotive gasoline at room temperature showed a corrosion rate below 5 µm per year in all cases. Such a value was considered negligible, since it corresponds to weight measurements comparable to the experimental error. Consequently, these immersion tests led to the conclusion that none of these fluids were corrosive to any of the specimens at room temperature.

The result is graphically evident in Figure 17, which compares the results with those previously presented for full immersion in saline water (NaCl 5%). It is clear that NaCl (5%) is a more corrosive environment than the other fluids, especially for additively manufactured AlSi10Mg and cast A356 components. In some of the test cases, high deviation of results was obtained due to the large amounts of corrosion products deposited on the samples.

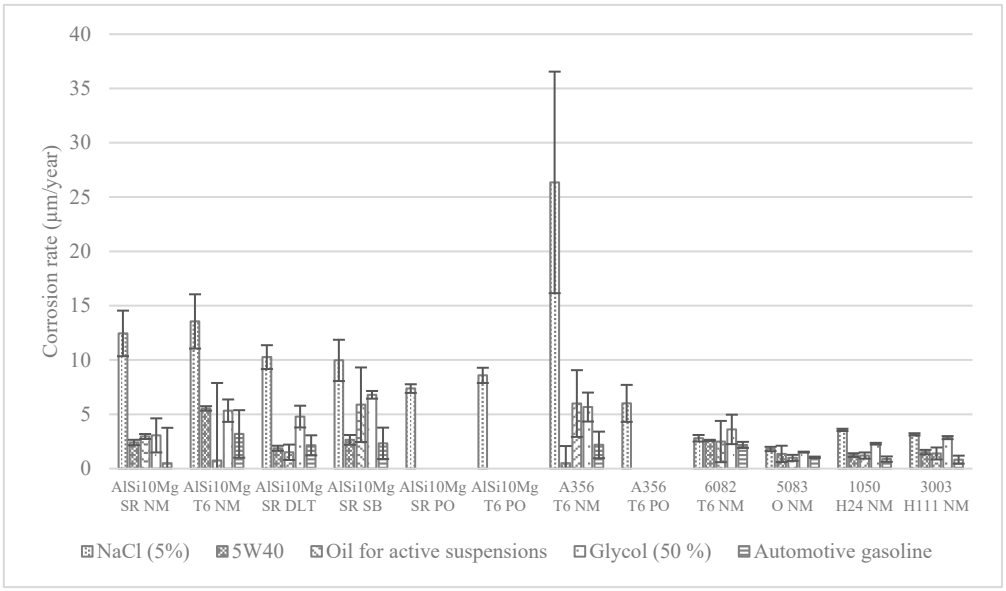

Figure 17. Corrosion rate comparison of the specimens immersed in the different fluids at room temperature for 30 days.

3.4. Immersion Tests in 5W40, Suspension Oil and Cooling Fluid at T = 90 °C

The immersion tests of the different specimens in glycol (50%), 5W40 and oil for active suspensions were repeated, again for 30 days, at a temperature of 90 °C in order to better simulate the operating temperature of these fluids in the vehicle and, thus, understand the true corrosion behaviour of the alloys in their working environment.

Again, no visible signs of corrosion were noticed on any sample surface, with the exception of the specimens immersed in glycol (50%). In this case, an oxide layer formed on the surfaces, regardless of the alloy or heat/surface treatment.

This phenomenon was partially confirmed by the corrosion rate calculation. As shown in Figure 18, glycol (50%) at 90 °C led to a generally higher corrosion rate in comparison to the other fluids. However, almost all values, with the exception of the AlSi10Mg_T6_NM specimens, were around or below 5µm per year and are, therefore, to be considered negligible.

The AlSi10Mg_T6_NM showed a surprisingly high corrosion rate value in all three fluids tested at high temperatures, although no corrosion products were present on the surface. The reason for this phenomenon is not clear. It is possible that a sufficiently long

stay at a high temperature promotes general and uniform corrosion over the entire surface of AlSi10Mg_T6_NM specimens. Again, corrosion may be favoured by the AlSi10Mg T6 microstructure described in the previous sections. The graphs in Figure 19a–c compare the results of the tests at room temperature and at 90 °C for 5W40 oil, oil for active suspensions and glycol (50%).

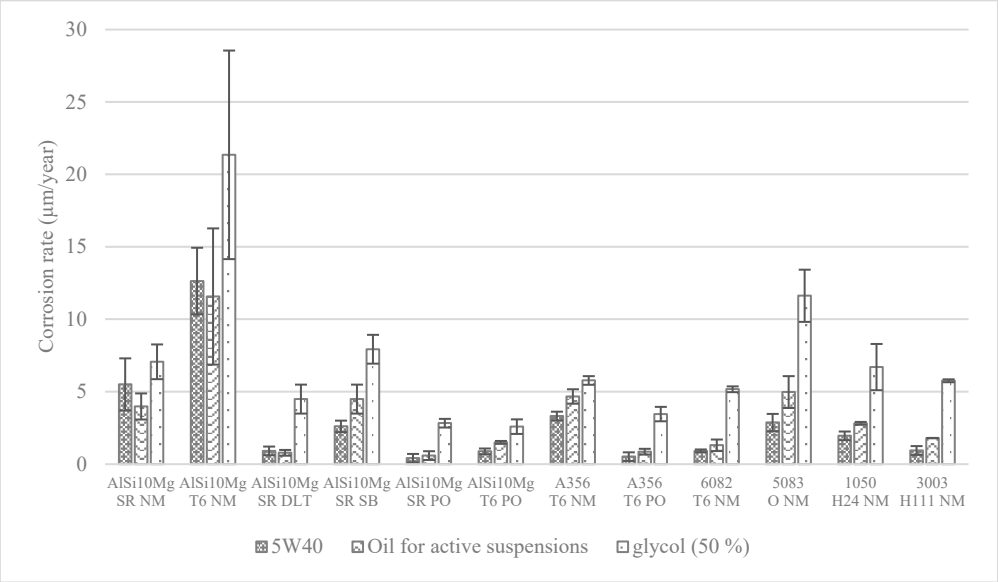

Figure 18. Corrosion rate comparison of the specimens immersed in glycol (50%), 5W40 and oil for active suspensions at 90 °C for 30 days.

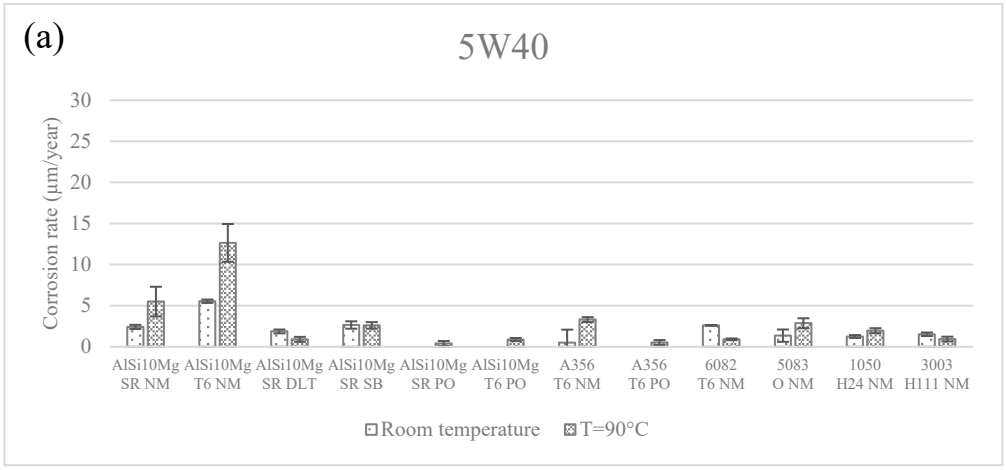

Figure 19. *Cont.*

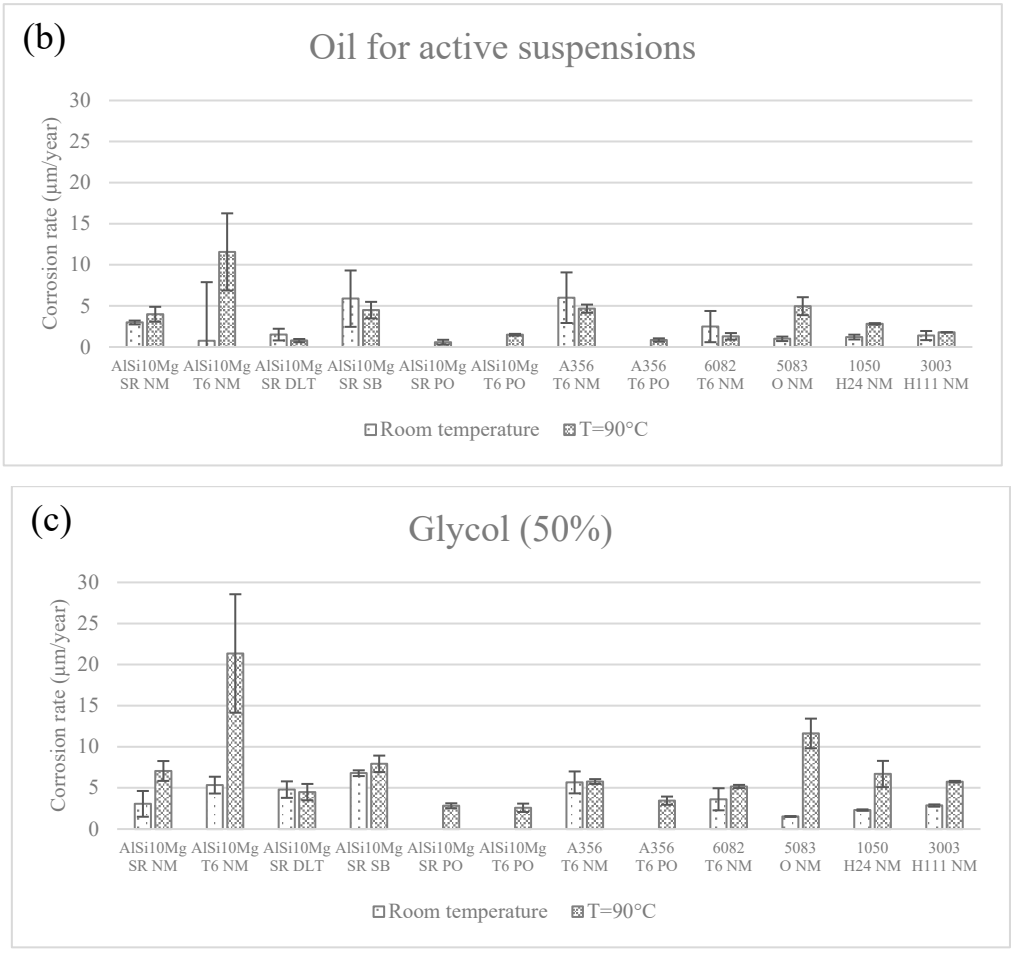

Figure 19. Corrosion rate comparison of the specimens immersed in (**a**) 5W40, (**b**) oil for active suspensions and (**c**) glycol 50% at 90 °C and at room temperature. With the exception of the AlSi10Mg_T6_NM specimens, all the other samples exhibit a negligible corrosion rate.

4. Conclusions

- The corrosion resistance of additively manufactured AlSi10Mg was compared with that of cast and wrought Al alloys, both in terms of qualitative inspections of corrosion phenomena and quantitative calculations of their corrosion rate.
- The corrosion behaviour of the AlSi10Mg produced using L-PBF was found to be strongly dependent on the heat treatment conditions. In the stress-relieved microstructure, corrosion proceeded along the melt pool borders, while the extremely fine grains and the presence of a continuous Si network in the melt pool core had a protective effect. The T6 treatment caused a reduction in the corrosion resistance, as the dispersed Si domains could not effectively protect the Al matrix.
- Both sand blasting and electrochemical machining guaranteed a slight improvement in corrosion behaviour compared to non-machined surfaces. The effect was even more pronounced in the case of polished specimens, where the smooth and passivated surface hindered corrosion initiation and propagation.
- In saline water, the corrosion rate measurements of the additively manufactured AlSi10Mg parts were lower than those of the cast specimens in the T6 condition. On the other hand, even in the optimum condition of a stress-relieved polished part, the corrosion behaviour obtained by AM did not match that obtained by plastic deformation.
- Fluids commonly used in the automotive sector did not significantly damage any of the aluminium specimens tested at room temperature. At a temperature of 90 °C, instead, the same environments became very critical for Alsi10Mg produced by AM,

especially when treated with T6. This surprisingly high corrosion rate should be the subject of further investigation.

Author Contributions: Conceptualization and methodology, A.G. and F.F.; validation, S.D.; formal analysis, C.C.; investigation, C.C.; data curation, S.D.; writing—original draft preparation, C.C.; writing—review and editing, S.D.; visualization, C.C.; supervision, A.G.; project administration, F.F. All authors have read and agreed to the published version of the manuscript.

Funding: This research received no external funding.

Data Availability Statement: The data presented in this study are available on request from the corresponding author.

Conflicts of Interest: The authors declare no conflict of interest. The funders had no role in the design of the study; in the collection, analyses or interpretation of data; in the writing of the manuscript; or in the decision to publish the results.

References

1. Gibson, I.; Rosen, D.; Stucker, B.; Khorasani, M. Powder Bed Fusion. In *Additive Manufacturing Technologies*; Springer International Publishing: Cham, Switzerland, 2021; pp. 125–170.
2. Frazier, W.E. Metal Additive Manufacturing: A Review. *J. Mater. Eng. Perform.* **2014**, *23*, 1917–1928. [CrossRef]
3. Kellens, K.; Mertens, R.; Paraskevas, D.; Dewulf, W.; Duflou, J.R. Environmental Impact of Additive Manufacturing Processes: Does AM Contribute to a More Sustainable Way of Part Manufacturing? *Procedia CIRP* **2017**, *61*, 582–587. [CrossRef]
4. Ford, S.; Despeisse, M. Additive manufacturing and sustainability: An exploratory study of the advantages and challenges. *J. Clean. Prod.* **2016**, *137*, 1573–1587. [CrossRef]
5. Bassoli, E.; Defanti, S.; Tognoli, E.; Vincenzi, N.; Degli Esposti, L. Design for Additive Manufacturing and for Machining in the Automotive Field. *Appl. Sci.* **2021**, *11*, 7559. [CrossRef]
6. Li, W.; Li, S.; Liu, J.; Zhang, A.; Zhou, Y.; Wei, Q.; Yan, C.; Shi, Y. Effect of heat treatment on AlSi10Mg alloy fabricated by selective laser melting: Microstructure evolution, mechanical properties and fracture mechanism. *Mater. Sci. Eng. A* **2016**, *663*, 116–125. [CrossRef]
7. Defanti, S.; Cappelletti, C.; Gatto, A.; Tognoli, E.; Fabbri, F. Boosting Productivity of Laser Powder Bed Fusion for AlSi10Mg. *J. Manuf. Mater. Process.* **2022**, *6*, 112. [CrossRef]
8. Liu, X.; Zhao, C.; Zhou, X.; Shen, Z.; Liu, W. Microstructure of selective laser melted AlSi10Mg alloy. *Mater. Des.* **2019**, *168*, 107677. [CrossRef]
9. Li, X.P.; Wang, X.J.; Saunders, M.; Suvorova, A.; Zhang, L.C.; Liu, Y.J.; Fang, M.H.; Huang, Z.H.; Sercombe, T.B. A selective laser melting and solution heat treatment refined Al–12Si alloy with a controllable ultrafine eutectic microstructure and 25% tensile ductility. *Acta Mater.* **2015**, *95*, 74–82. [CrossRef]
10. Maamoun, A.H.; Elbestawi, M.; Dosbaeva, G.K.; Veldhuis, S.C. Thermal post-processing of AlSi10Mg parts produced by Selective Laser Melting using recycled powder. *Addit. Manuf.* **2018**, *21*, 234–247. [CrossRef]
11. Padovano, E.; Badini, C.; Pantarelli, A.; Gili, F.; D'Aiuto, F. A comparative study of the effects of thermal treatments on AlSi10Mg produced by laser powder bed fusion. *J. Alloys Compd.* **2020**, *831*, 154822. [CrossRef]
12. Aboulkhair, N.T.; Maskery, I.; Tuck, C.; Ashcroft, I.; Everitt, N.M. The microstructure and mechanical properties of selectively laser melted AlSi10Mg: The effect of a conventional T6-like heat treatment. *Mater. Sci. Eng. A* **2016**, *667*, 139–146. [CrossRef]
13. Chen, H.; Zhang, C.; Jia, D.; Wellmann, D.; Liu, W. Corrosion Behaviors of Selective Laser Melted Aluminum Alloys: A Review. *Metals* **2020**, *10*, 102. [CrossRef]
14. Al Nur, M.; Khan, A.A.; Dev Sharma, S.; Kaiser, M.S. Electrochemical corrosion performance of Si-doped Al-based automotive alloy in 0.1 M NaCl solution. *J. Electrochem. Sci. Eng.* **2022**, *12*, 565–576. [CrossRef]
15. Benoit, M.J.; Ogunsanya, I.G.; Winkler, S.; Worswick, M.J.; Wells, M.A.; Hansson, C.M. Internal Corrosion of Warm Formed Aluminum Alloy Automotive Heat Exchangers. *J. Mater. Eng. Perform.* **2021**, *30*, 2876–2889. [CrossRef]
16. Gu, X.; Zhang, J.; Fan, X.; Dai, N.; Xiao, Y.; Zhang, L.-C. Abnormal corrosion behavior of selective laser melted AlSi10Mg alloy induced by heat treatment at 300 °C. *J. Alloys Compd.* **2019**, *803*, 314–324. [CrossRef]
17. Yang, Y.; Chen, Y.; Zhang, J.; Gu, X.; Qin, P.; Dai, N.; Li, X.; Kruth, J.-P.; Zhang, L.-C. Improved corrosion behavior of ultrafine-grained eutectic Al-12Si alloy produced by selective laser melting. *Mater. Des.* **2018**, *146*, 239–248. [CrossRef]
18. Prashanth, K.G.; Debalina, B.; Wang, Z.; Gostin, P.F.; Gebert, A.; Calin, M.; Kühn, U.; Kamaraj, M.; Scudino, S.; Eckert, J. Tribological and corrosion properties of Al–12Si produced by selective laser melting. *J. Mater. Res.* **2014**, *29*, 2044–2054. [CrossRef]
19. Fathi, P.; Mohammadi, M.; Duan, X.; Nasiri, A.M. A comparative study on corrosion and microstructure of direct metal laser sintered AlSi10Mg_200C and die cast A360.1 aluminum. *J. Mater. Process. Technol.* **2018**, *259*, 1–14. [CrossRef]
20. Leon, A.; Aghion, E. Effect of surface roughness on corrosion fatigue performance of AlSi10Mg alloy produced by Selective Laser Melting (SLM). *Mater. Charact.* **2017**, *131*, 188–194. [CrossRef]

21. Simeunovic, S.; Jung, C.; Mory, D.; Seiler, D.; de Wild, M. Investigating dry electro-chemical polishing of titanium structures. *Curr. Dir. Biomed. Eng.* **2021**, *7*, 77–80. [CrossRef]
22. *ANSI H35.1/H35.1(M)-2017*; American National Standard Alloy and Temper Designation Systems for Aluminum. ANSI (American National Standards Institute): Washington, DC, USA, 2017.
23. *ASTM G31-72*; Standard Practice for Laboratory Immersion Corrosion Testing of Metals. ASTM International: West Conshohocken, PE, USA, 2004.
24. Liao, B.; Ma, S.; Zhang, S.; Li, X.; Quan, R.; Wan, S.; Guo, X. Fructus cannabis protein extract powder as a green and high effective corrosion inhibitor for Q235 carbon steel in 1 M HCl solution. *Int. J. Biol. Macrom.* **2023**, *239*, 124358. [CrossRef] [PubMed]
25. Liao, B.; Luo, Z.; Wan, S.; Chen, L. Insight into the anti-corrosion performance of Acanthopanax senticosus leaf extract as eco-friendly corrosion inhibitor for carbon steel in acidic medium. *J. Ind. Eng. Chem.* **2023**, *117*, 238–246. [CrossRef]
26. *ASTM G1-03(2017)e1*; Standard Practice for Preparing, Cleaning, and Evaluating Corrosion Test Specimens. ASTM International(American Society for Testing and Materials): West Conshohocken, PE, USA, 2017.
27. Amir, B.; Grinberg, E.; Gale, Y.; Sadot, O.; Samuha, S. Influences of platform heating and post-processing stress relief treatment on the mechanical properties and microstructure of selective-laser-melted AlSi10Mg alloys. *Mater. Sci. Eng. A* **2021**, *822*, 141612. [CrossRef]
28. Aboulkhair, N.T.; Everitt, N.M.; Ashcroft, I.; Tuck, C. Reducing porosity in AlSi10Mg parts processed by selective laser melting. *Addit. Manuf.* **2014**, *1–4*, 77–86. [CrossRef]
29. Kang, N.; Coddet, P.; Chen, C.; Wang, Y.; Liao, H.; Coddet, C. Microstructure and wear behavior of in-situ hypereutectic Al–high Si alloys produced by selective laser melting. *Mater. Des.* **2016**, *99*, 120–126. [CrossRef]
30. Liu, Y.J.; Liu, Z.; Jiang, Y.; Wang, G.W.; Yang, Y.; Zhang, L.C. Gradient in microstructure and mechanical property of selective laser melted AlSi10Mg. *J. Alloys Compd.* **2018**, *735*, 1414–1421. [CrossRef]
31. Ding, X.; Wang, L. Heat transfer and fluid flow of molten pool during selective laser melting of AlSi10Mg powder: Simulation and experiment. *J. Manuf. Process.* **2017**, *26*, 280–289. [CrossRef]
32. Wei, P.; Wei, Z.; Chen, Z.; Du, J.; He, Y.; Li, J.; Zhou, Y. The AlSi10Mg samples produced by selective laser melting: Single track, densification, microstructure and mechanical behavior. *Appl. Surf. Sci.* **2017**, *408*, 38–50. [CrossRef]
33. Thijs, L.; Kempen, K.; Kruth, J.-P.; Van Humbeeck, J. Fine-structured aluminium products with controllable texture by selective laser melting of pre-alloyed AlSi10Mg powder. *Acta Mater.* **2013**, *61*, 1809–1819. [CrossRef]
34. Aboulkhair, N.T.; Tuck, C.; Ashcroft, I.; Maskery, I.; Everitt, N.M. On the Precipitation Hardening of Selective Laser Melted AlSi10Mg. *Metall. Mater. Trans. A* **2015**, *46*, 3337–3341. [CrossRef]
35. Leon, A.; Shirizly, A.; Aghion, E. Corrosion Behavior of AlSi10Mg Alloy Produced by Additive Manufacturing (AM) vs. Its Counterpart Gravity Cast Alloy. *Metals* **2016**, *6*, 148. [CrossRef]